Article

Deriving VIIRS High-Spatial Resolution Water Property Data Over Coastal and Inland Waters Using Deep Convolutional Neural Network

Xiaoming Liu [1,2,*] **and Menghua Wang** [1]

1   NOAA National Environmental Satellite, Data, and Information Service, Center for Satellite Applications and Research, 5830 University Research Court, College Park, MD 20746, USA; Menghua.Wang@noaa.gov

2   Cooperative Institute for Research in the Atmosphere at Colorado State University, Fort Collins, CO 80523, USA

*   Correspondence: Xiaoming.Liu@noaa.gov

Abstract: The Visible Infrared Imaging Radiometer Suite (VIIRS) onboard the Suomi National Polar-orbiting Partnership (SNPP) satellite has been a reliable source of ocean color data products, including five moderate (M) bands and one imagery (I) band normalized water-leaving radiance spectra $nL_w(\lambda)$. The spatial resolutions of the M-band and I-band $nL_w(\lambda)$ are 750 m and 375 m, respectively. With the technique of convolutional neural network (CNN), the M-band $nL_w(\lambda)$ imagery can be super-resolved from 750 m to 375 m spatial resolution by leveraging the high spatial resolution features of I1-band $nL_w(\lambda)$ data. However, it is also important to enhance the spatial resolution of VIIRS-derived chlorophyll-a (Chl-a) concentration and the water diffuse attenuation coefficient at the wavelength of 490 nm ($K_d(490)$), as well as other biological and biogeochemical products. In this study, we describe our effort to derive high-resolution $K_d(490)$ and Chl-a data based on super-resolved $nL_w(\lambda)$ images at the VIIRS five M-bands. To improve the network performance over extremely turbid coastal oceans and inland waters, the networks are retrained with a training dataset including ocean color data from the Bohai Sea, Baltic Sea, and La Plata River Estuary, covering water types from clear open oceans to moderately turbid and highly turbid waters. The evaluation results show that the super-resolved $K_d(490)$ image is much sharper than the original one, and has more detailed fine spatial structures. A similar enhancement of finer structures is also found in the super-resolved Chl-a images. Chl-a filaments are much sharper and thinner in the super-resolved image, and some of the very fine spatial features that are not shown in the original images appear in the super-resolved Chl-a imageries. The networks are also applied to four other coastal and inland water regions. The results show that super-resolution occurs mainly on pixels of Chl-a and $K_d(490)$ features, especially on the feature edges and locations with a large spatial gradient. The biases between the original M-band images and super-resolved high-resolution images are small for both Chl-a and $K_d(490)$ in moderately to extremely turbid coastal oceans and inland waters, indicating that the super-resolution process does not change the mean values of the original images.

Keywords: VIIRS; ocean color; chlorophyll-a; super-resolution; convolutional neural network

1. Introduction

Ocean color environmental data records (EDRs, or Level-2 data) from the Visible Infrared Imaging Radiometer Suite (VIIRS) onboard the Suomi National Polar-orbiting Partnership (SNPP) satellite provide high quality ocean color remote sensing data source for science research and ocean environment monitoring. The normalized water-leaving radiance spectra $nL_w(\lambda)$ [1–3] of the five moderate (M) bands (M1–M5 at wavelengths of 410, 443, 486, 551, and 671 nm) with a spatial resolution of 750 m are the fundamental ocean color products derived from VIIRS. In addition, VIIRS also provides high-spatial resolution visible imagery (I) bands with 375 m resolution, and especially $nL_w(\lambda)$ of the

I1 band at the wavelength of 638 nm has been used recently [4]. Based on the VIIRS-derived $nL_w(\lambda)$ spectra, chlorophyll-a (Chl-a) concentration [5–8]; water diffuse attenuation coefficient at the wavelength of 490 nm $K_d(490)$ [9]; as well as some other parameters, e.g., inherent optical properties (IOPs) [10–12], are also derived. Ocean color EDRs are processed from the sensor data records (SDR) using the Multi-Sensor Level-1 to Level-2 (MSL12) ocean color data processing system [13], which is designed to process ocean color data for multiple sensors from various satellites [14]. In fact, ocean color EDRs are one of the primary product suites of VIIRS instruments on board the Joint Polar Satellite System (JPSS) series [13,15].

The VIIRS I-band spatial resolution (375 m) is exactly twice that of the M-bands' (750 m). Wang and Jiang (2018) [4] reported that there is more detailed spatial information of optical water properties in the I1 band $nL_w(638)$ images than that of the M-band images, especially over turbid coastal oceans and inland waters. It is noted that the I-band and M-band radiances are accurately co-registered as they are recorded at exactly the same time and location, and with identical sensor-solar geometry. Therefore, the spatial features of $nL_w(\lambda)$ at the M-band and I-band images are highly correlated, and it is possible to leverage the I-band high-spatial resolution structure to super-resolve M-band $nL_w(\lambda)$ images [16]. Super-resolving a coarse resolution image to a fine resolution has been a very active field of research, as various satellite measurements have become available in recent years, and it is also known as image fusion in remote sensing [17–22]. A brief review of recent literature in image fusion methods can be found in [16]. Among them, the machine learning approach has made significant advancement in recent years, especially with the development of the deep convolutional neural network (CNN). As a class of artificial neural networks, CNN has been a dominant method in visual imagery analysis and computer vision [23]. Indeed, Liu and Wang (2021) [16] used the deep CNN to extract high-spatial resolution content from the VIIRS I-band images, and leverage it to super-resolve M-band images. Specifically, five VIIRS M-bands $nL_w(\lambda)$ images are super-resolved with different networks trained separately so that the performance of the network of different bands can be evaluated. The results show that the fine spatial structures are significantly enhanced in super-resolved $nL_w(\lambda)$ images, and they look shaper than the original images. The biases between the original M-band $nL_w(\lambda)$ images and super-resolved images are small for all bands, but less errors were found in the super-resolved $nL_w(\lambda)$ images at the red and green bands compared with those at the blue bands. The results also show that the networks are able to super-resolve M-band $nL_w(\lambda)$ images by utilizing the correlations between the I1-band and M-band $nL_w(\lambda)$ images [16].

While $nL_w(\lambda)$ spectra at the VIIRS five M-bands are primary parameters directly derived from VIIRS measurements [13], Chl-a and $K_d(490)$ are important ocean color products for ocean biological and biogeochemical properties that have been widely used by science and user communities for various applications. In fact, the initial objective for an ocean color satellite mission, the Coastal Zone Color Scanner (CZCS), is to derive global Chl-a distributions [24,25]. Indeed, Chl-a data are the primary product for all the follow on satellite ocean color missions [26], such as the Sea-viewing Wide Field-of-view Sensor (SeaWiFS) [27], the Moderate Resolution Imaging Spectroradiometer (MODIS) [28,29], the Medium-Resolution Imaging Spectrometer (MERIS) [30], VIIRS [13,15], the Ocean and Land Colour Instrument (OLCI) [31], and the Second-Generation Global Imager [32]. Therefore, it is desirable to also super-resolve VIIRS Chl-a and $K_d(490)$ to 375 m resolution, particularly over turbid coastal oceans and inland waters. In this study, we further develop and evaluate high-spatial resolution Chl-a and $K_d(490)$ products based on super-resolved $nL_w(\lambda)$ images of the VIIRS five M-bands. Specifically, high-spatial resolution Chl-a and $K_d(490)$ are derived from super-resolved $nL_w(\lambda)$ spectra using the same Chl-a and $K_d(490)$ algorithms [7,9] as implemented in the MSL12 ocean color data processing system [13]. High-spatial resolution Chl-a and $K_d(490)$ products are compared and evaluated with the original data of 750 m resolution.

In the previous study, Liu and Wang (2021) [16] trained and evaluated neural networks for super-resolving VIIRS M-bands $nL_w(\lambda)$ using ocean color data from the Bohai Sea and Baltic Sea separately, and found that the networks trained from these two regions are equivalent. However, waters over neither the Bohai Sea nor Baltic Sea are extremely turbid. Therefore, the networks trained from these two regions lack proper skills to sharpen the ocean color $nL_w(\lambda)$ images over highly turbid waters. Turbid coastal oceans and inland waters usually contain a large amount of sediment, which has significant effects on the optical property of the water column. Turbid waters in the world oceans are usually located near the world's major river estuaries [33,34], for example, Yangtze River Estuary, La Plata River Estuary, Amazon River Estuary, Meghna River Estuary, and so on. In the coastal region, the water turbidity is highly dynamic and closely associated with the atmosphere, ocean, and land variability, such as cyclones, algae blooms, and flood-driven river plumes. High-resolution Chl-a and $K_d(490)$ images in the coastal region can help to understand water column property and benthic processes such as primary productivity, coral reef ecosystem, nutrient dynamics, and river dynamics. In this study, the data from the La Plata River Estuary are added into the training dataset, so that the networks are more robust to deal with highly turbid waters. Therefore, the objectives of this study are twofold, i.e., first, to retrain the network with the dataset of the La Plata River Estuary; and second, to develop and evaluate the high-spatial resolution Chl-a and $K_d(490)$ with newly trained networks. The rest of the paper is organized as follows. The deep CNN models, Chl-a and $K_d(490)$ algorithms, as well as datasets used for training, evaluation, and testing, are described in Section 2. The results of network training, evaluation, and testing for Chl-a and $K_d(490)$ products are presented in Section 3. Finally, discussions and conclusion are provided in Section 4.

2. Data and Methods

2.1. VIIRS Ocean Color EDR Data

We use the VIIRS-SNPP ocean color EDR (or Level-2) data processed by the NOAA Ocean Color Team (https://www.star.nesdis.noaa.gov/socd/mecb/color/, accessed on 14 May 2021) using the MSL12 ocean color data processing system [13,35]. MSL12 is the NOAA's official ocean color data processing system for VIIRS, and it has been used to process satellite ocean optical, biological, and biogeochemical data using various atmospheric correction algorithms [35]. The atmospheric correction algorithms include the near-infrared (NIR) approach [1,2,36], the shortwave infrared (SWIR) algorithm [3], and the NIR–SWIR combined algorithm [37]. In particular, the NIR–SWIR-based atmospheric correction in MSL12 has been shown to significantly improve satellite ocean color data over global open oceans and turbid coastal/inland waters [38–41]. In this study, the NIR–SWIR combined atmospheric correction algorithm [37] is used to derive VIIRS-SNPP ocean color $nL_w(\lambda)$ spectra.

As an important result of the atmospheric correction in the ocean color data processing [1–3], normalized water-leaving radiance $nL_w(\lambda)$ spectra [2,42–44] measure the outgoing radiances backscattered from oceans/waters at different wavelengths. VIIRS-SNPP ocean color product data include $nL_w(\lambda)$ spectra at the seven M-bands (750 m) at wavelengths of 410, 443, 486, 551, 671, 745, and 862 nm, and one I-band (375 m) $nL_w(\lambda)$ at 638 nm. It was reported that the high resolution $nL_w(638)$ can reveal more detailed fine features of water optical, biological, and biogeochemical properties than those with M-band $nL_w(\lambda)$ [4]. In fact, the red I-band $nL_w(638)$ data can be used in various ocean color applications to study fine spatial resolution dynamic features, particularly over turbid coastal oceans and inland waters [16,45,46].

VIIRS ocean color products also include Chl-a and $K_d(490)$, which are frequently used by users to monitor ocean environment, e.g., ocean/water biological productivity [47,48] and harmful algal bloom (HAB) monitoring [49,50]. VIIRS Chl-a and $K_d(490)$ data are derived from $nL_w(\lambda)$ spectra [13,35]. Specifically, the $K_d(490)$ algorithm is a hybrid of clear ocean (standard) model and turbid ocean model, so that the $K_d(490)$ product for both clear

and turbid ocean waters can be accurately retrieved [9]. The VIIRS Chl-a algorithm uses the ocean color index (OCI) method, which has been proven to be more stable and accurate for clear (low Chl-a) oceans [6,7]. In this study, these two $K_d(490)$ and Chl-a algorithms are implemented in the super-resolution application (Python) to generate 375 m resolution products, so that the super-resolved $K_d(490)$ and Chl-a can be compared with original data.

The I1 band $nL_w(638)$ data have strong signals in coastal oceans and inland waters, but generally have very weak signals in open oceans. Therefore, in this study, we use ocean color data derived from VIIRS-SNPP in coastal oceans and inland waters, including the Bohai Sea, Baltic Sea, La Plata River Estuary, Great Lakes, Chesapeake Bay, and Gulf of Mexico. A single VIIRS-SNPP ocean color EDR file (granule) comprises an ~85 seconds of orbit segment spanning 48 scans. Each individual scan contains 32 and 16 rows for the I-band and M-band, respectively, with one row for each detector. Individual rows contain a total of 6400 and 3200 samples in the I-band and M-band data, respectively. Consequently, each VIIRS ocean color EDR granule has a total of 6400 × 1536 and 3200 × 768 image elements in the I-band and M-band data, respectively, which cover a ground swath of approximately 3060 km wide.

2.2. Convolution Neural Networks and Training

Because the spatial features in VIIRS I1-band $nL_w(638)$ images are highly correlated with those in M-bands, Liu and Wang (2021) [16] employed the deep CNN to obtain the high-frequency content from $nL_w(638)$, and use it to super-resolve M-band $nL_w(\lambda)$ imageries. In their study, VIIRS ocean color data over the Bohai Sea and Baltic Sea were used to train the networks for super-resolution of coastal ocean color $nL_w(\lambda)$ images. However, a significant discrepancy is found between the original M-band $nL_w(\lambda)$ images and super-resolved images when the networks are applied to extremely turbid ocean areas. The poor performance of the network over extremely turbid waters is attributed to the limitation of the training dataset: it only contains ocean color data from the Bohai Sea and Baltic Sea, which are not highly turbid waters. Therefore, the networks lack the proper skills to super-resolve images of extremely turbid oceans.

In this study, VIIRS ocean color data from the extremely turbid La Plata River Estuary are included in the training dataset. We retrain the same CNN models [51], and the network architecture is shown in Figure 1, and is briefly described as follows. The M-band $nL_w(\lambda)$ spectra are first bilinearly upsampled to the same dimension as the I1 band, $nL_w(638)$. The upsampled M-band $nL_w(\lambda)$ are then concatenated with $nL_w(638)$ along the horizontal axis, and serve as the input of the network. It is the concatenation step that adds the high-spatial resolution I-band information to the procedure. The input data go into the first convolution layer, a rectified linear unit (ReLU), iteration of residual blocks, the last convolution layer, and an additive skip connection at the end. For the convolution layers, we use 128 feature maps and 3 × 3 convolution kernels, as using a small kernel size can benefit from weight sharing and reduction in computational costs [23]. In addition, zero-padding is used so that the convolved image has the same dimension as the input image. The ReLU function simply truncates all negative values to zeroes in the output. The module of residual block employs the popular ResNet architecture [52], which uses skip connections to make it faster to train very deep networks.
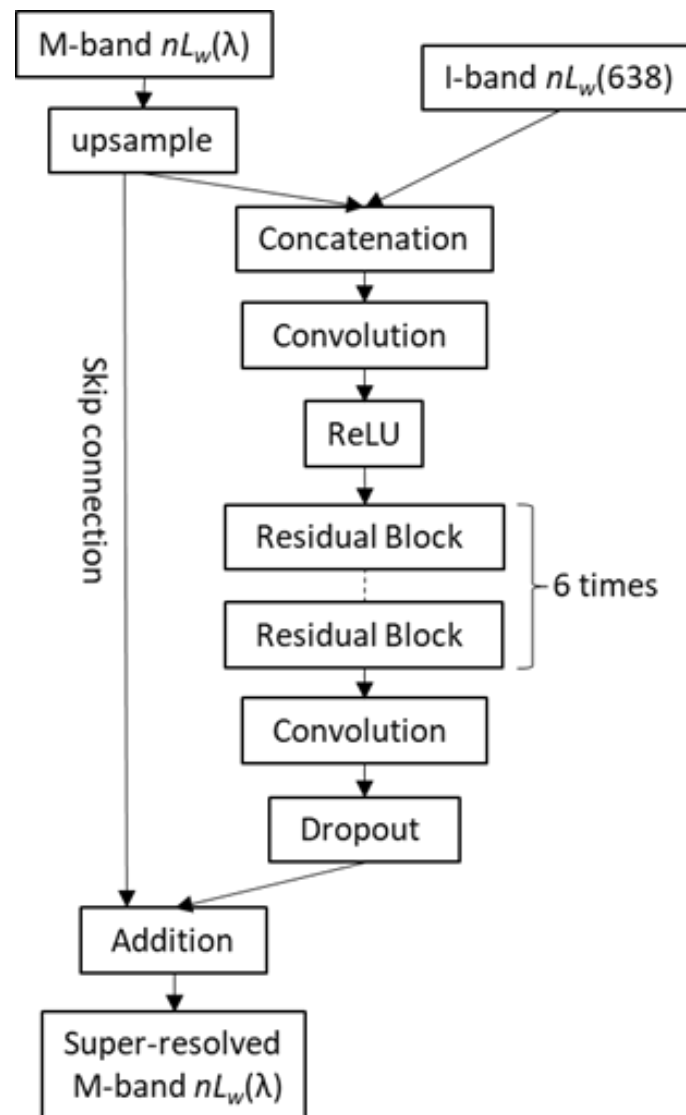
Figure 1. Architecture of the convolution neural network. ReLu, rectified linear unit.

As in Liu and Wang (2021) [16], we retrain five networks with one network for each M-band $nL_w(\lambda)$. Network training requires a large amount of data as a training dataset, but we do not have 375 m resolution $nL_w(\lambda)$ data as ground truth. Therefore, we need to make an assumption that super-resolving $nL_w(\lambda)$ images from 750 m to 375 m resolution (original scale) is self-similar to super-resolving images on a degraded 1500 m to 750 m scale [16,51]. With this assumption, we train the networks on a degraded 1500 m to 750 m scale, i.e., VIIRS M-band $nL_w(\lambda)$ images are synthetically downsampled from 750 m to 1500 m, and used as coarse-resolution inputs, and the original images are treated as the ground truth. The networks trained with synthetic data have been proven to work well to super-resolve $nL_w(\lambda)$ images on the original scale [16]. Forty-five granules of VIIRS ocean color EDR data (Table 1) are used as the training dataset, and they are preprocessed into small patches of 32×32 pixels. We use 90% of patches for training the model weights and 10% for validation. The network and training are implemented in the Keras frameworks (https://github.com/keras-team/keras, accessed on 14 May 2021) with TensorFlow as backend.

Table 1. List of Visible Infrared Imaging Radiometer Suite (VIIRS) environmental data record (EDR) granules of the Bohai Sea, Baltic Sea, and La Plata River Estuary used for training the network.

|	Baltic Sea		Bohai Sea		La Plata River Estuary	
	Granule	**Date**	**Granule**	**Date**	**Granule**	**Date**
1	V2019070042852	11 Mar 2019	V2015213113614	01 Aug 2015	V2020019175116	19 Jan 2020
2	V2019073051140	14 Mar 2019	V2015215105822	03 Aug 2015	V2020046174522	15 Feb 2020
3	V2019073051305	14 Mar 2019	V2015216103927	04 Aug 2015	V2020057173912	26 Feb 2020
4	V2019074045411	15 Mar 2019	V2015221104550	09 Aug 2015	V2020062174536	02 Mar 2020
5	V2019075043516	16 Mar 2019	V2015223114859	11 Aug 2015	V2020063172640	03 Mar 2020
6	V2019084050531	25 Mar 2019	V2015225111108	13 Aug 2015	V2020073173926	13 Mar 2020
7	V2019090045259	31 Mar 2019	V2015227103444	15 Aug 2015	V2020083175048	23 Mar 2020
8	V2019091043404	01 Apr 2019	V2015228115523	16 Aug 2015	V2020084173317	24 Mar 2020
9	V2019100050545	10 Apr 2019	V2015229113502	17 Aug 2015	V2020095172707	04 Apr 2020
10	V2019106045313	16 Apr 2019	V2015229113627	17 Aug 2015	V2020109180347	18 Apr 2020
11	V2019116050558	26 Apr 2019	V2015230111606	18 Aug 2015	V2020110174451	19 Apr 2020
12	V2019121051222	01 May 2019	V2015230111731	18 Aug 2015	V2020111172557	20 Apr 2020
13	V2019126051846	06 May 2019	V2015231105836	19 Aug 2015	V2020131175128	10 May 2020
14	V2019127045950	07 May 2019	V2015232103942	20 Aug 2015	V2020133171337	12 May 2020
15	V2019143050004	23 May 2019	V2015235112355	23 Aug 2015	V2020137173857	16 May 2020

3. Results

3.1. Training Networks

The performance of the deep CNN relies heavily on the training datasets. VIIRS ocean color data over the Bohai Sea and Baltic Sea were used to train the networks for super-resolution of coastal ocean color images [16]. The maximum $K_d(490)$ values of the Bohai Sea and Baltic Sea are usually ~2.0 m^{-1} and ~4.0 m^{-1}, respectively. However, in extremely turbid coastal and inland lake regions, for example, the La Plata River Estuary [53], $K_d(490)$ values can reach up to ~6.0–7.0 m^{-1} [54]. Therefore, super-resolution networks trained with the Bohai Sea and Baltic Sea data could not be able to accurately super-resolve $nL_w(\lambda)$ images over extremely turbid waters. We have to re-train the CNNs by also including $nL_w(\lambda)$ spectra data from highly turbid water regions such as La Plata River Estuary in the training datasets.

Forty-five granules (Table 1) of VIIRS-SNPP ocean color data from the Bohai Sea, Baltic Sea, and La Plata River Estuary were used to re-train five networks (one for $nL_w(\lambda)$ at each M-band), and they are referred to as networks with *new training*. In comparison, the networks trained previously with only the Bohai Sea and Baltic Sea data [16] are referred to as *old training*. The difference between the *new training* and *old training* is only in the training dataset, while the CNN model and the settings are kept the same. It is noted that the ocean color satellite images contain lots of missing data owing to clouds, high sun glint, high sensor-zenith angle, and so on. In our treatment of the missing data in the process of CNN, we assign the mean of all valid pixels in the images to all missing data points.

Figure 2 shows the comparison of the original images (750 m resolution) with super-resolved images (375 m resolution) of both *old training* and *new training* for $nL_w(443)$, $nL_w(551)$, and $nL_w(671)$, as well as $K_d(490)$ and Chl-a on 27 February 2020, in the La Plata River Estuary. It can be seen that, for $nL_w(443)$ and $nL_w(671)$, the original images are essentially the same as the super-revolved images with both *old training* and *new training*. However, for $nL_w(551)$, the radiances with *old training* (Figure 2g) are obviously underestimated in the La Plata River Estuary (color looks more orange), while the data from *new training* (Figure 2l) are significantly improved and look very similar to the original image. As the training dataset of *old training* contains only data from the Bohai Sea and Baltic Sea, the networks of *old training* do not have the skills to super-resolve the images of highly turbid water regions. Consequently, Chl-a data are underestimated with *old training* (the color looks more greenish in the La Plata River Estuary in Figure 2j), as Chl-a are derived from $nL_w(443)$, $nL_w(486)$, and $nL_w(551)$ [7]. The

training dataset of *new training* includes the data from the extremely turbid La Plata River Estuary, so Chl-a are significantly improved (Figure 2o). On the other hand, K_d(490) data are more correlated to nL_w(671) [9], so the differences between using *old training* and *new training* are generally small (Figure 2i,n).
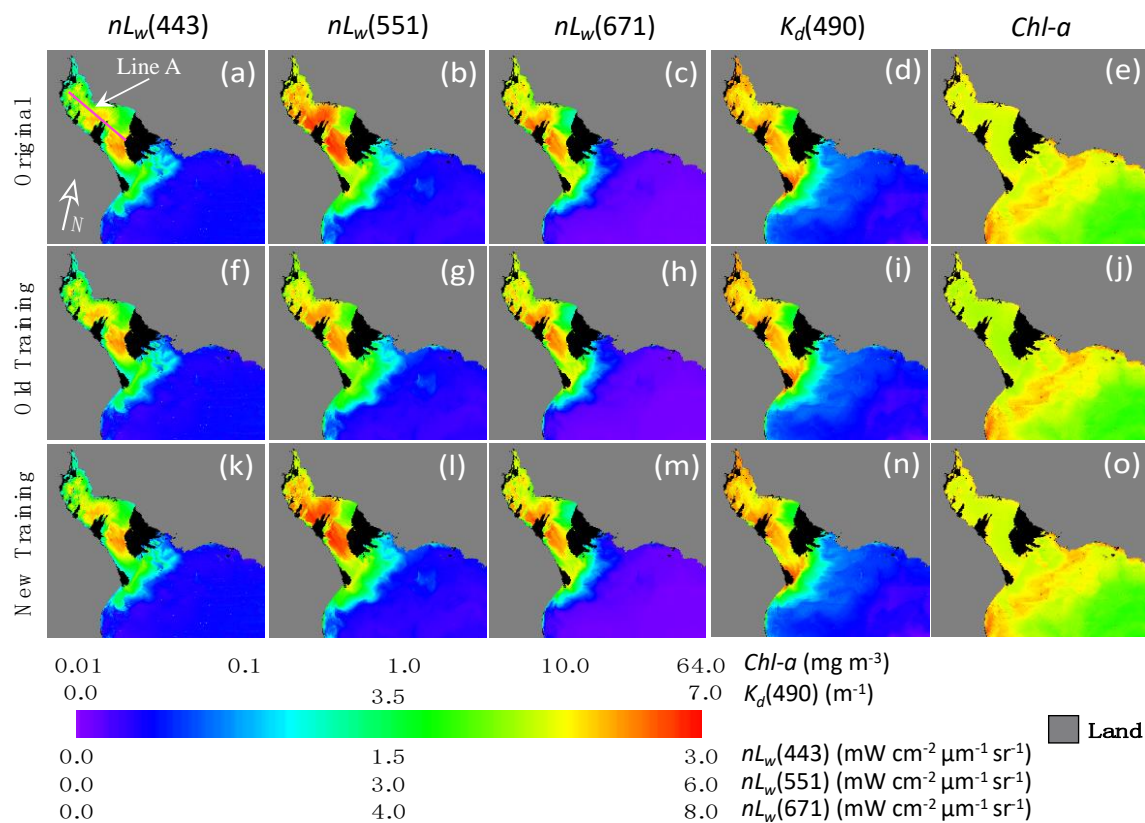
Figure 2. Visible Infrared Imaging Radiometer Suite (VIIRS)-derived original images (**a**–**e**), super-resolved images with *old training* (**f**–**j**), and super-resolved images with *new training* (**k**–**o**) of nL_w(443), nL_w(551), nL_w(671), K_d(490), and Chl-a in the La Plata River Estuary on 27 February 2020. Note that a line A is marked in Figure 2a for further analysis.

To quantitatively evaluate the difference between the results of using *old training* and *new training*, Figure 3 shows the line plots of nL_w(443), nL_w(551), nL_w(671), K_d(490), and Chl-a along line A (pink line) marked in Figure 2a. As we can see in Figure 3, nL_w(671) values are ~7.0 mW cm^{-2} µm^{-1} sr^{-1} (Figure 3a) and K_d(490) are generally ~6.0 m^{-1} (Figure 3b), which indicate that the region is indeed extremely turbid in the La Plata River Estuary [54]. In addition, nL_w(551) values are also abnormally high (~5.0 mW cm^{-2} µm^{-1} sr^{-1}), and they are higher than those in the Bohai Sea and Baltic Sea (~4.0 mW cm^{-2} µm^{-1} sr^{-1}) [16]. Therefore, the networks trained in the Bohai Sea and Baltic Sea (*old training*) underestimate nL_w(551) by ~7% in the La Plata River Estuary. Figure 3c and d shows the percent difference, i.e., 100 × (super-resolved − original)/original, of Chl-a and K_d(490) with *old training* (blue cross) and *new training* (red circle) along line A noted in Figure 2a. As a result, Chl-a concentrations are underestimated by ~21% with old training (Figure 3c), while K_d(490) are only underestimated by ~1% with *old training* (Figure 3d). With *new training*, both K_d(490) and Chl-a values are significantly improved with essentially zero biases. Therefore, it is concluded that including the data from highly turbid water regions in the training dataset (i.e., covering all possible data ranges) is necessary for the network models to accurately super-resolve satellite-measured K_d(490) and Chl-a images in various coastal and inland water environments.
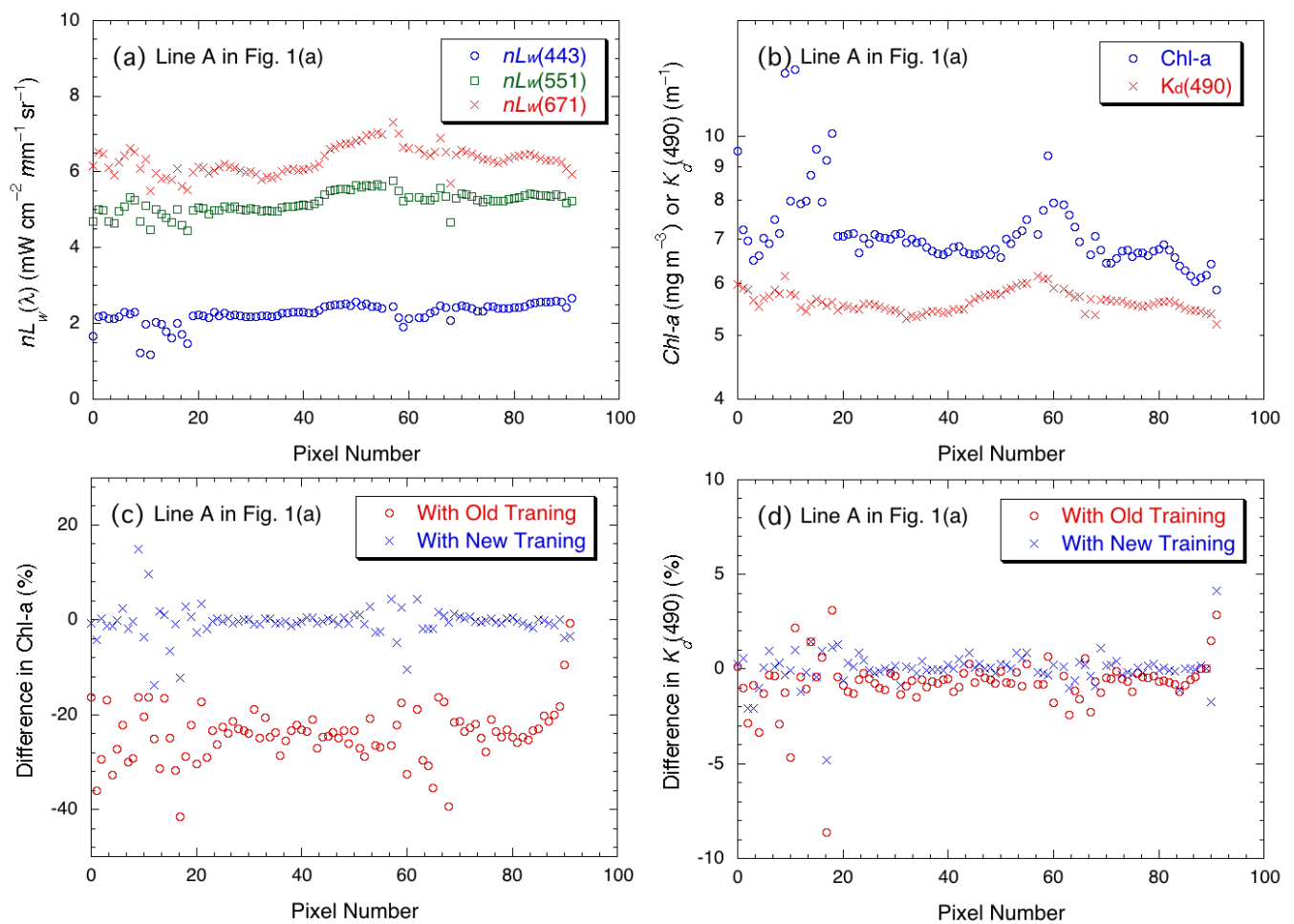
Figure 3. Line plots (along line A in Figure 2a) for (**a**) $nL_w(443)$, $nL_w(551)$, and $nL_w(671)$; (**b**) $K_d(490)$ and Chl-a; (**c**) percent difference of Chl-a with *old training* (blue cross) and *new training* (red circle); and (**d**) percent difference of $K_d(490)$ with *old training* (blue cross) and *new training* (red circle).

3.2. Network Validation

As described in the previous section, the network training assumes that super-resolving $nL_w(\lambda)$ images from 750 m to 375 m resolution are self-similar to super-resolving images on a degraded 1500 m to 750 m scale. This assumption requires that the $nL_w(\lambda)$ relationships between bands of different spatial resolutions are self-similar within the relevant scale range, i.e., the transfer of spatial details in $nL_w(\lambda)$ from high-spatial resolution to low-spatial resolution bands does not depend on the spatial resolution itself, but depends only on the relative resolution difference. In fact, the assumption is supported by the literature on self-similarity in image analysis [55,56], and has been proven to be effective in image super-resolution applications [16,51]. Following the same validation procedure by Liu and Wang (2021) [16], quantitative evaluations of the networks of *new training* are performed by super-resolving $nL_w(\lambda)$ images on a degraded 1500 m to 750 m scale, and the original 750 m spatial resolution $nL_w(\lambda)$ data are treated as ground truth to evaluate the super-resolved $nL_w(\lambda)$ images. The networks obtained from *new training* are applied on down-sampled 1500 m resolution images in the Baltic Sea (Granule V2015226105214), Bohai Sea (Granule V2019105051208), and La Plata River Estuary (Granule V2020058172016), and the super-resolved 750-m-resolution data are compared pixel-by-pixel with the original $nL_w(\lambda)$ images for validation. The results show that the mean, median, and standard deviation (STD) of the super-resolved/original $nL_w(\lambda)$ ratio in the three regions on average

are 0.995, 0.997, and 0.056, respectively. Therefore, the performance is consistent with the validation results tested previously in the Baltic Sea and Bohai Sea [16].

As the goal of this study is to super-resolve $K_d(490)$ and Chl-a images, we also evaluate the performance of the networks on $K_d(490)$ and Chl-a data on a degraded 1500 m to 750 m scale. Specifically, super-resolved 750 m $nL_w(\lambda)$ data generated above from the down-sampled 1500 m resolution are used to calculate $K_d(490)$ and Chl-a data (super-resolved). Pixel-by-pixel comparisons between the super-resolved and original $K_d(490)$ and Chl-a data of the same resolution are evaluated. The results show that the mean, median, and STD of the super-resolved/original $K_d(490)$ ratio in the three regions on average are 1.003, 1.001, and 0.077, respectively. For Chl-a, the mean, median, and STD of the super-resolved/original ratio in the three regions on average are 0.995, 0.998, and 0.096, respectively. For both parameters, the biases between the super-resolved and original data are quite small, but their STD values are larger than those in $nL_w(\lambda)$. In addition, the performance of super-resolved $K_d(490)$ and Chl-a in the La Plata River Estuary shows no significant difference than that in the Baltic Sea and Bohai Sea.

3.3. Super-Resolved $K_d(490)$ and Chl-a in the Baltic Sea

The networks with *new training* are used to super-resolve to VIIRS M-band $nL_w(\lambda)$ images at the Baltic Sea from the spatial resolution of 750 m to 375 m. As the Baltic Sea is not a highly turbid region, the difference between using *new training* and *old training* can be neglected. The super-resolved $nL_w(\lambda)$ images of the VIIRS five M-bands in the Baltic Sea have been evaluated in the previous study [16]. In this study, we mainly focus on high-resolution $K_d(490)$ and Chl-a products, which are derived from the super-resolved $nL_w(\lambda)$ spectra. Figure 4 shows the original $K_d(490)$ and Chl-a images and super-resolved images of an EDR granule acquired on 14 August 2015 (Granule V2015226105214) in the Baltic Sea. It can be seen that the super-resolved $K_d(490)$ image (Figure 4b) is much sharper than the original one (Figure 4a), and has more detailed fine spatial structures. For example, the green color filaments of high $K_d(490)$ crossing line B (purple line) marked in Figure 4a look blurry (750 m spatial resolution), while those filaments are sharpened with clearer edges in Figure 4b (375 m spatial resolution). In addition, the fuzzy features on the side of the n-shape structure to the left end of line B in Figure 4a are replaced with many clear finer features in Figure 4b. Similar changes can be seen in other locations of the $K_d(490)$ image. Some of the thick and blurry features in the original image are enhanced with two or more separated filaments in the super-resolved image, while some other very faint features in the original $K_d(490)$ image are clearly highlighted with sharp lines in the super-resolved $K_d(490)$ image. However, it should be noted that the general pattern and color of those features are the same in Figure 4a,b, which shows that the super-resolution process does not change the mean value of those features.

Similarly, fine spatial structures of Chl-a are also enhanced in the super-resolved images (Figure 4c,d). Because the Chl-a algorithm uses $nL_w(\lambda)$ at the blue and green bands, which is less correlated to $nL_w(638)$ [16], the pattern of the Chl-a features looks different from those of $K_d(490)$ (as expected for the two different products). The high-concentration Chl-a filaments (yellow and red) are much sharper and thinner in the super-resolved image (Figure 4d), and some of the finer features that are not available in the original Chl-a image now appear in the super-resolved Chl-a image. As shown in $K_d(490)$ images, the super-resolving process does not change the mean value of these Chl-a features, so the color of these Chl-a features is generally the same in the super-resolved and original images.
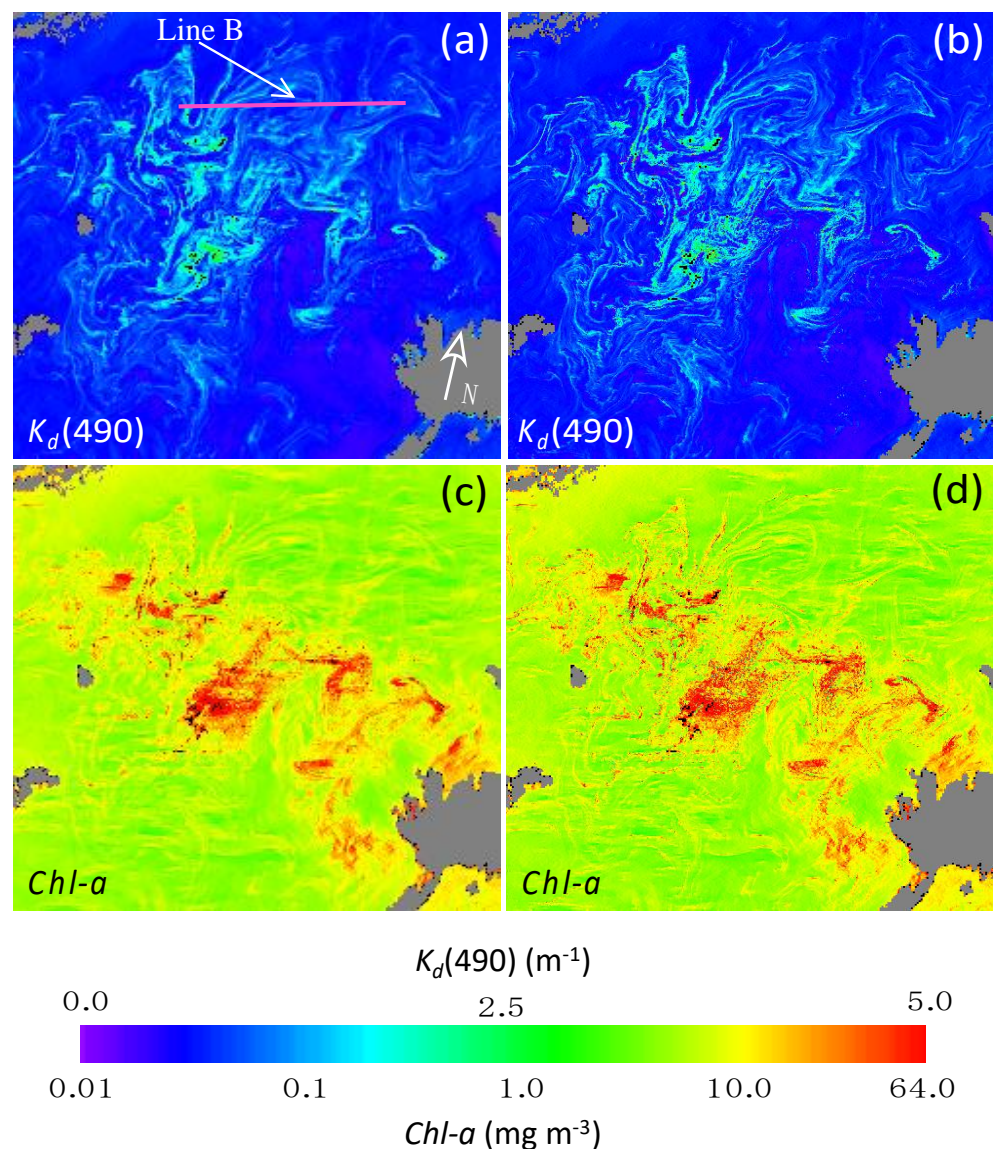
Figure 4. Comparisons of ocean color images of the Baltic Sea on 14 August 2015, for (**a**) original $K_d(490)$, (**b**) super-resolved $K_d(490)$, (**c**) original Chl-a, and (**d**) super-resolved Chl-a. Note that line B is marked in Figure 4a for further analysis.

The enhancement of the super-resolved $K_d(490)$ images is further evaluated quantitatively at the pixel level. Figure 5 shows the line plots of the super-resolved and original $K_d(490)$ images along line B (pink line in Figure 4a). The original and super-resolved $K_d(490)$ values are compared to $nL_w(638)$ along the line to demonstrate the performance of the network. The differences between $K_d(490)$ and $nL_w(638)$ are usually quite large in magnitude in the Baltic Sea. However, we mostly care about the $K_d(490)$ changes along line B for the purpose of performance evaluation. Therefore, we normalized $nL_w(638)$ and $K_d(490)$ values along line B to the value of the first point on the left (by taking the ratio), so that we can easily compare their variations along the line. Figure 5a shows the line plots of the original and super-resolved normalized $K_d(490)$ values along line B, as well as the normalized $nL_w(638)$ values on the same line (scale noted in the right). It can be seen that the super-resolved (normalized) $K_d(490)$ images (red line) have more high-frequency variations than the original (normalized) $K_d(490)$ images (blue line). These high-frequency variations correspond to the fine spatial features in the super-resolved $K_d(490)$ images. It is also noted that the high-frequency (normalized) $K_d(490)$ variations are mostly consistent with those in $nL_w(638)$ (green line). In fact, the high correlation coefficient of 0.9661 between

super-resolved $K_d(490)$ and $nL_w(638)$ indicates that the high-frequency variations in $K_d(490)$ have been successfully transferred from the super-resolved M-band, which essentially learned from the I1 band ($nL_w(638)$).
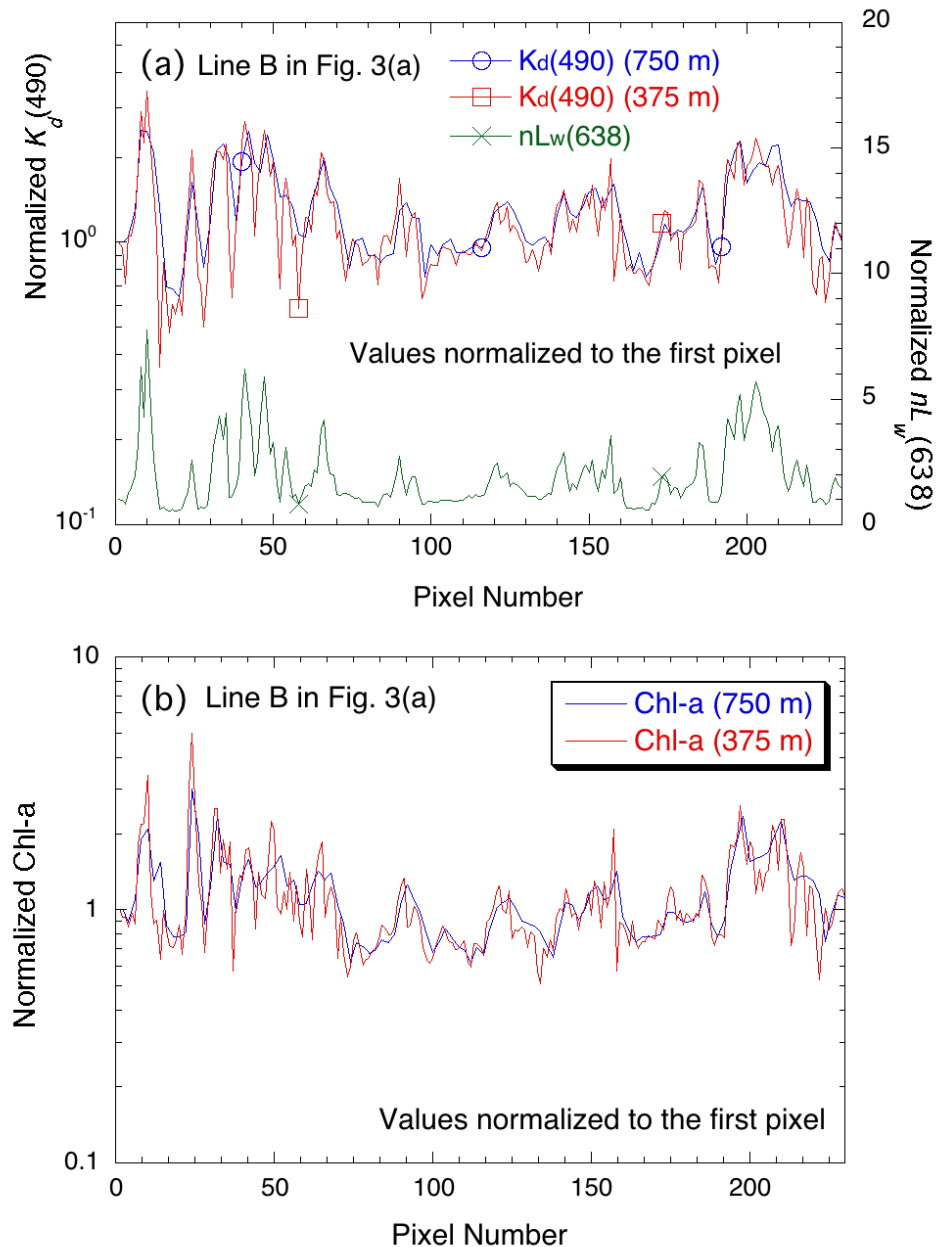
Figure 5. Line plots (along line B in Figure 4a) for (**a**) original and super-resolved normalized $K_d(490)$ in comparison with normalized $nL_w(638)$ and (**b**) original and super-resolved normalized Chl-a. Note that all values are normalized to the left-most point on line B in Figure 4a.

Similarly, Figure 5b shows line plots of the original and super-resolved Chl-a values (normalized) along line B. As shown in the $K_d(490)$ results, there are more high-frequency variations in the super-resolved Chl-a line plot (red) than in the original one (blue). Compared with the super-resolved $K_d(490)$, the super-resolved Chl-a is less correlated with $nL_w(638)$ (correlation coefficient of 0.6283). It can be seen that, although the low-frequency variations of Chl-a are not in line with $nL_w(638)$ (green line in Figure 5a), the network can still add high-frequency variations on top of low-frequency variations in the super-resolved Chl-a image.

Furthermore, we quantitatively compare the original $K_d(490)$ and Chl-a images with the super-resolved images in the Baltic Sea. As each pixel in the original image corresponds to four pixels in the super-resolved image, the density-scatter plots of the super-resolved images versus original images by corresponding pixels for $K_d(490)$ and Chl-a are shown in Figure 6, and they are both very close to the 1:1 line. The statistics of the ratio between the original $K_d(490)$ (or Chl-a) images and the corresponding super-resolved images are also calculated. The mean ratios of the super-resolved/original $K_d(490)$ and Chl-a image are 0.997 and 1.008, respectively, indicating that the biases between the original $K_d(490)$ (or Chl-a) images and the corresponding super-resolved images are very small ($<\sim$1%). The STD values of the super-resolved/original image ratios for $K_d(490)$ and Chl-a are 0.045 and 0.062, respectively. In fact, these variations are mostly caused by the added high-resolution features in the super-resolved $K_d(490)$ and Chl-a images.

(a)　　　　　　　　　　　　　　**(b)**
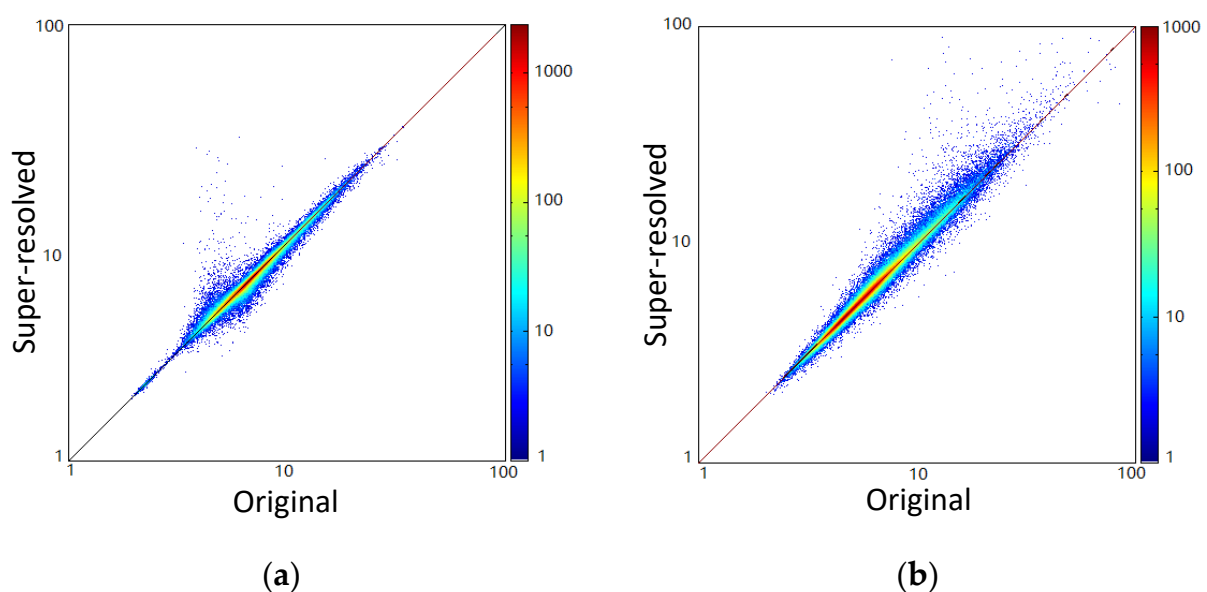
Figure 6. Scatter-density plots of the super-resolved versus original images of (**a**) $K_d(490)$ and (**b**) Chl-a in the Baltic Sea on 14 August 2015.

3.4. Tests in Other Coastal and Inland Waters

The performance of the networks is also tested in four coastal and inland water regions, i.e., the Bohai Sea, Chesapeake Bay, Lake Erie, and Gulf of Mexico, which include both sediment-dominate and phytoplankton-dominate waters. The networks with *new training* are applied to VIIRS ocean color data in the four regions to super-resolve $nL_w(\lambda)$ images of five M-bands, and then high-resolution $K_d(490)$ and Chl-a are derived from the super-resolved $nL_w(\lambda)$ spectra for evaluations.

3.4.1. The Bohai Sea Region

The Bohai Sea is a major marginal sea of approximately 78,000 km^2 on the east coast of China. In the Bohai Sea, the ocean dynamics and water properties are dominated primarily by river runoff, semidiurnal/diurnal tides, and seasonal monsoons, and so on [57]. As the Yellow River flows into the Bohai Sea, both sediments and phytoplankton blooms have significant effects on the water optical property in this region [58]. Shi et al. (2011) [59] also reported that the spring-neap tide can make significant $K_d(490)$ variations in the Bohai Sea, as the tidal current plays an important role on sediment resuspension. In addition, the $K_d(490)$ features can also be enhanced by the sand ridges on the bottom of the eastern Bohai Sea [58]. Figure 7 shows $K_d(490)$ and Chl-a images in the Bohai Sea on 9 September 2018, as well as the ratio of the super-resolved/original image. $K_d(490)$ data have a large dynamic range in the region, as its maximum value can reach as high as $\sim$4 m^{-1}

(Figure 7a). With the strong influence of the tidal current and wind waves [59], there are lots of fine dynamic features in satellite ocean color images. For example, the finger-shaped features on the bottom of the $K_d(490)$ image are induced by the sand ridges on the ocean floor [60]. These features are significantly enhanced by the super-resolved $K_d(490)$ image. To compare the original $K_d(490)$ images with the super-resolved images, we calculate the pixel-by-pixel super-resolved/original $K_d(490)$ ratio (Figure 7b). It can be seen in most parts of the image where $K_d(490)$ are uniform, and ratios of super-resolved/original are close to 1.0 (green color). In the locations with some significant $K_d(490)$ features, ratios of super-resolved/original deviate from 1.0. For example, the edges of the finger-shaped feature induced by sand ridges [60] are clearly modified, so that the feature edges are sharpened in the super-resolved image. The mean and STD of the super-resolved/original $K_d(490)$ ratio for the region are 1.003 and 0.056, respectively (Table 2), which indicate that there are little biases between the super-resolved and original image. The Chl-a image of the Bohai Sea looks quite uniform (Figure 7c). Consequently, there is less enhancement in the super-resolved Chl-a image (Figure 7d). The mean and STD of the super-resolved/original Chl-a ratio for the region are 0.999 and 0.060, respectively.
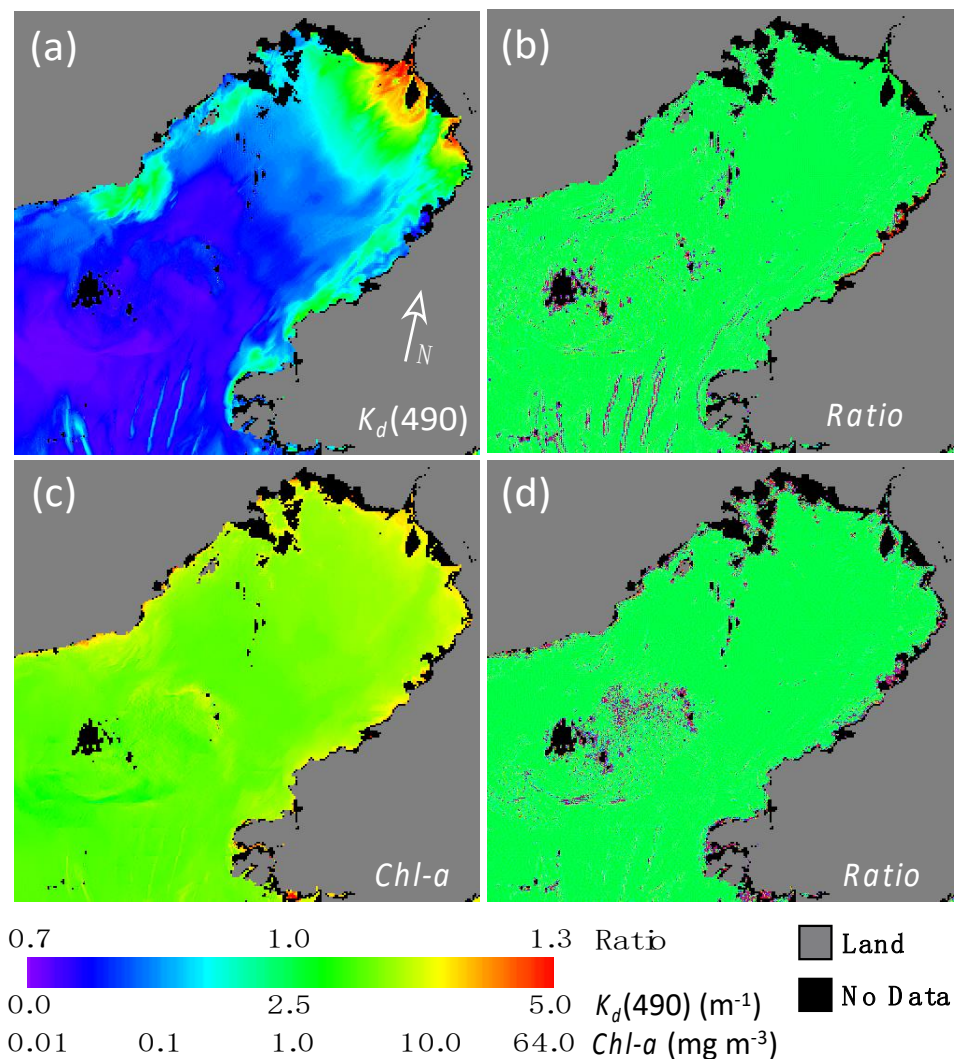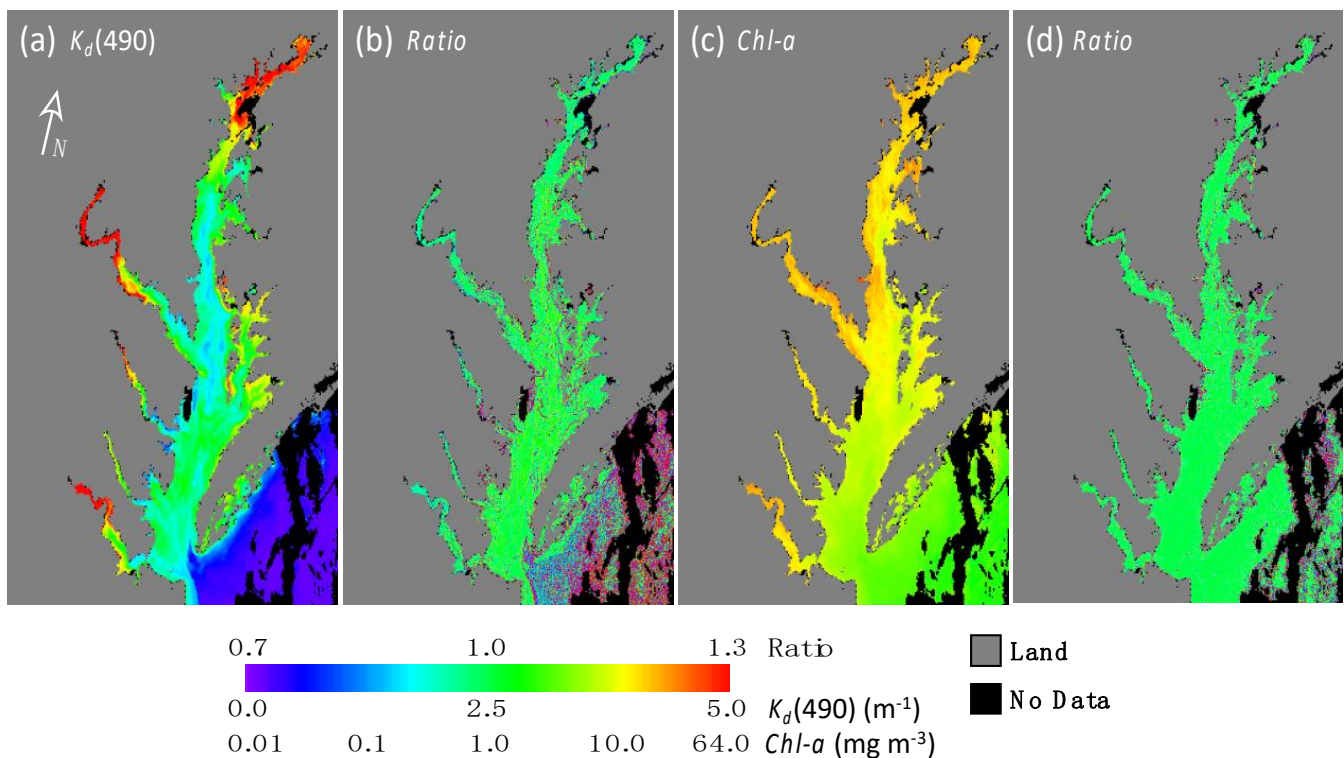

Figure 7. (**a**) Original $K_d(490)$, (**b**) ratio of super-resolved/original $K_d(490)$, (**c**) original Chl-a, and (**d**) ratio of super-resolved/original Chl-a for a case in the Bohai Sea on 9 September 2018.

Table 2. The statistics of the super-resolved/original ratio for K_d(490) and Chl-a in the Bohai Sea, Chesapeake Bay, Lake Erie, and Gulf of Mexico.

Product	Bohai Sea			Chesapeake Bay			Lake Erie			Gulf of Mexico		
	Mean	Median	STD	Mean	Median	STD	Mean	Median	STD	Mean	Median	STD
K_d**(490)**	1.003	1.000	0.056	1.010	1.000	0.111	0.998	1.000	0.076	1.002	1.000	0.066
Chl-a	0.999	1.000	0.060	1.004	1.000	0.094	0.995	0.997	0.080	1.015	1.000	0.128

### 3.4.2. The Chesapeake Bay Region

The Chesapeake Bay is the largest estuary in the United States, and one of the most productive water bodies in the world. There are about 150 rivers, creeks, and streams flowing into the Chesapeake Bay, and the top five largest rivers, Susquehanna, Potomac, Rappahannock, York, and James rivers, contribute ~90% of discharge. As a large amount of freshwater (~2300 m^3 s^{-1} on average) is discharged into the Chesapeake Bay, the dissolved and particulate materials can have a significant effect on the water property [61], and strongly influences phytoplankton production in the bay [48]. In addition, tidal forcing also plays an important role in sediment, biological, and geological processes in the Chesapeake Bay [62]. The upper Chesapeake Bay is extremely turbid because of the estuarine turbidity maximum (ETM) of the Susquehanna River [9,63]. Figure 8 shows K_d(490) and Chl-a images acquired on 3 March 2018, Granule V2018062175339, as well as the ratio of the super-resolved/original image in the Chesapeake Bay. It is noted that the K_d(490) value is so high (~5 m^{-1}) in the upper Chesapeake Bay (Figure 8a) that, with *old training*, nL_w(551) data are usually underestimated by ~4%, and Chl-a are generally underestimated by ~9%. The networks with *new training* work quite well; the super-resolved/original ratios for K_d(490) (Figure 8b) and Chl-a (Figure 8d) are both close to 1.0 (green color) in the upper Chesapeake Bay. Figure 8a also shows lots of K_d(490) features in the main stem of the Chesapeake Bay as well as in the tributaries. In general, it is much more turbid in the tributaries than in the main stem, as shown in Figure 8a. In the middle Chesapeake Bay, K_d(490) has the minimum in the center of the main stem, and gradually increases to the east and west shorelines. The super-resolution of all these water turbidity features is very important for routine monitoring of the Chesapeake Bay environment. It can be seen in Figure 8b that the super-resolution process is performed on these features with a significant K_d(490) gradient all around the Chesapeake Bay and the tributaries. On the other hand, Chl-a are generally uniform except in the middle bay region where the phytoplankton bloom is found on the west side of the Chesapeake Bay (Figure 8c). The super-resolution of the Chl-a is mainly performed in the middle bay (Figure 8d). In fact, as shown in Table 2, the mean values of the super-resolved/original ratios in K_d(490) and Chl-a are 1.010 and 1.004, respectively.

Figure 8. (**a**) Original $K_d(490)$, (**b**) ratio of super-resolved/original $K_d(490)$, (**c**) original Chl-a, and (**d**) ratio of super-resolved/original Chl-a for a case in the Chesapeake Bay on 3 March 2018.

3.4.3. Lake Erie

Lake Erie, the southern most of the Great Lakes, is generally not extremely turbid ($K_d(490) < {\sim}3$ m^{-1}), except for the west side of the lake [64,65]. However, there are often significant water quality issues owing to rapid growth of algae, which is mainly caused by runoff of fertilizer and manure spread on large farm fields [66–68]. These problems not only threaten the lake's ecosystem, but also the economic activities of the surrounding areas. Indeed, Lake Erie provides a primary drinking water source, and supports many recreational, tourism, and fishery activities. In addition, although most algae blooms in Lake Erie are harmless, the blue-green algae *Microcystis* produce toxins, and have harmful effects on human, birds, marine mammals, fish, and local economies [68,69]. Figure 9 shows $K_d(490)$ and Chl-a images of Lake Erie on 29 April 2018 (Granule V2018119182603). There are some turbid features ($K_d(490) > {\sim}2.0$ m^{-1}) mainly on the west side of the lake, but for most area of the lake, waters are non-turbid (or relatively clear, $K_d(490) < {\sim}1.0$ m^{-1}) (Figure 9a). Figure 9b shows the super-resolved/original ratio of $K_d(490)$ in Lake Erie. It can be seen that differences of the super-resolved and original $K_d(490)$ images are small for most pixels, except for the feature edges. The Chl-a image looks quite uniform (Figure 9c), and there are less Chl-a feature enhancements than those in the super-resolution of $K_d(490)$ image (Figure 9d). The mean values of the super-resolved/original ratio in $K_d(490)$ and Chl-a are 0.998 and 0.995 (Table 2), indicating that the super-resolution process does not change the general values of the original $K_d(490)$ and Chl-a images.
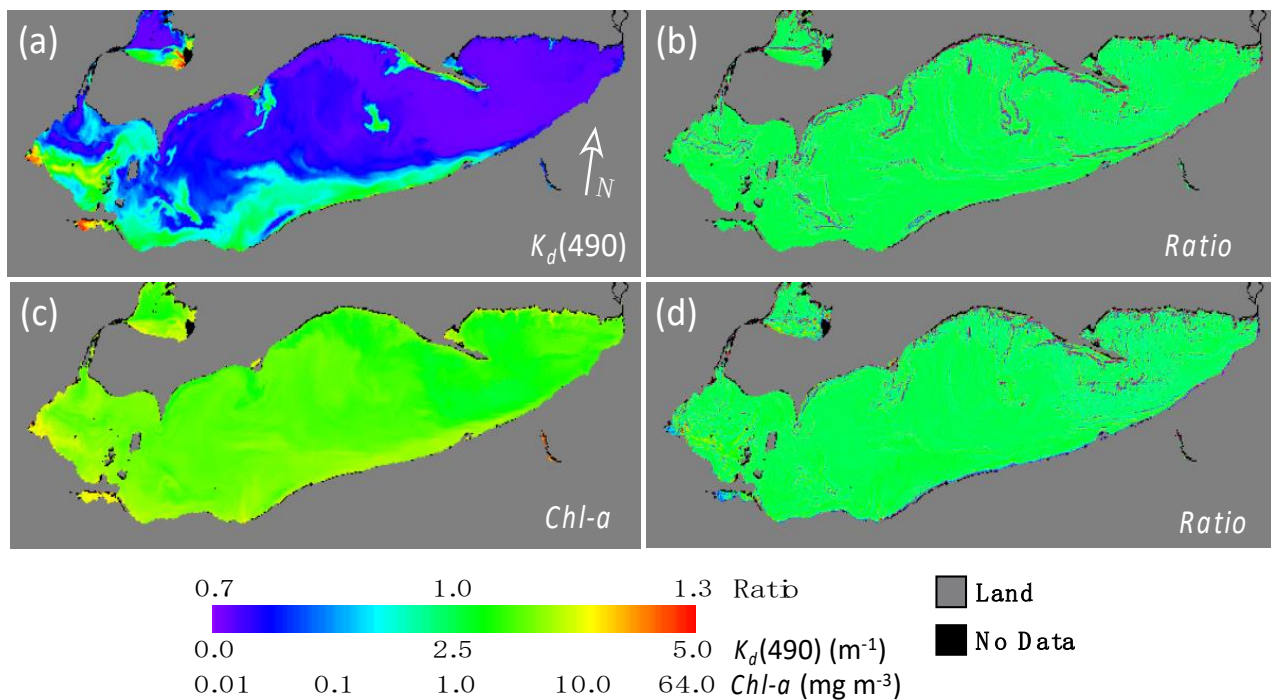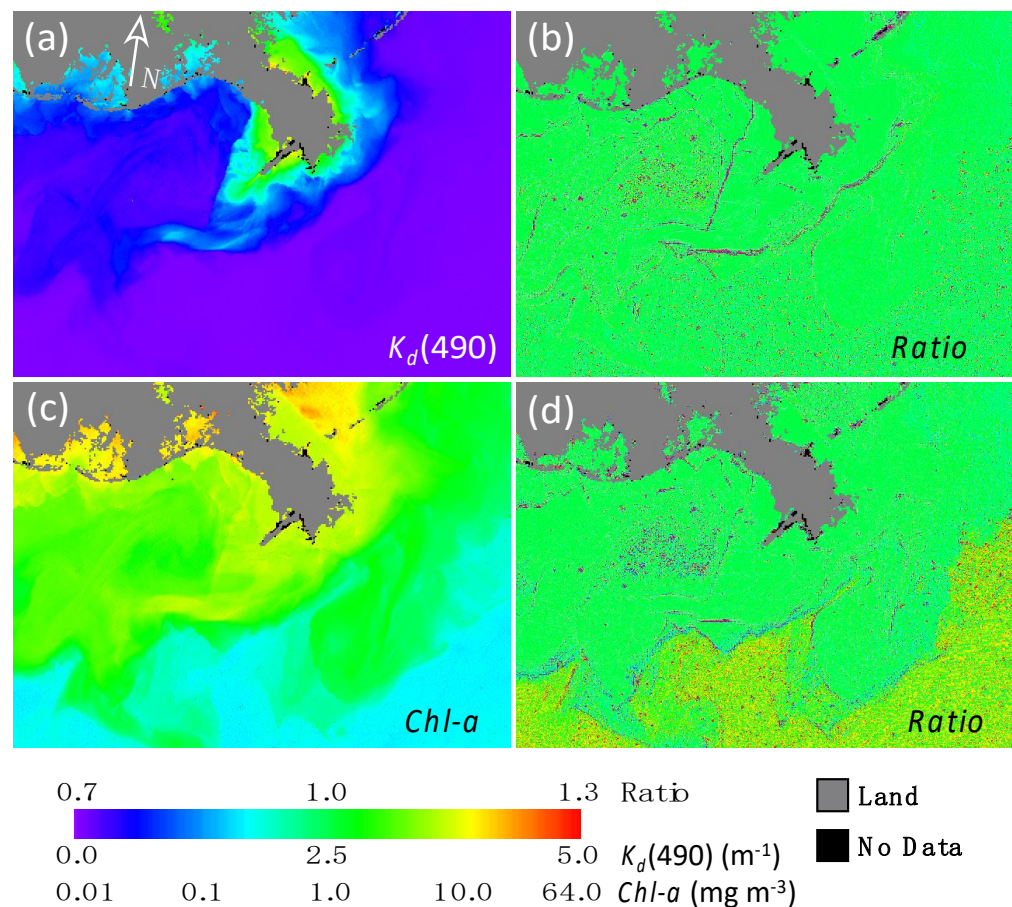
Figure 9. (**a**) Original $K_d(490)$, (**b**) ratio of super-resolved/original $K_d(490)$, (**c**) original Chl-a, and (**d**) ratio of super-resolved/original Chl-a for a case in Lake Erie on 29 April 2018.

3.4.4. The Gulf of Mexico Region

As the fourth longest river in the world (~6300 km), the Mississippi River discharges at a speed of 18,400 m^3 s^{-1} on average [70], and carries ~230 million tons of sediment into the Gulf of Mexico annually [71]. In the meantime, the Mississippi River brings a significant amount of nutrients into the Gulf of Mexico each year. As river plumes have significant effects on coastal marine ecosystems, including nutrient dynamics, biological productivity, water quality, and pollution hazards [72], high-resolution ocean color imageries can significantly benefit routine monitoring and understanding of river plume dynamics. Figure 10 shows the $K_d(490)$ and Chl-a images of 19 November 2019 (Granule V2019323185429), which cover the turbid Mississippi River plume. As shown in Figure 10a, waters are usually highly turbid ($K_d(490) > $ ~2.5 m^{-1}) around the Mississippi River Delta, but the water is clear in the open ocean. There are some finer features on the boundary between the turbid and clear waters. Figure 10b also shows that there are significant super-resolution enhancements on the turbid–clear water boundaries, and on some coastal features as well. The Chl-a image provides similar features to those of $K_d(490)$ around the Mississippi River Delta (Figure 10c), and the enhancement in the super-resolved image mainly occurs on the edge of these features. The mean values of the super-resolved/original ratios in $K_d(490)$ and Chl-a are 1.002 and 1.015, respectively, in the Gulf of Mexico region (Table 2).

Figure 10. (**a**) Original $K_d(490)$, (**b**) ratio of super-resolved/original $K_d(490)$, (**c**) original Chl-a, and (**d**) ratio of super-resolved/original Chl-a for a case in the Gulf of Mexico region on 19 November 2019.

In summary, from the results of the previous four examples, both $K_d(490)$ and Chl-a images in the turbid coastal oceans and inland waters show many enhanced fine spatial features. While Chl-a images look relatively more uniform than $K_d(490)$, significant super-resolution enhancements occur in both images. This is particularly useful for turbid coastal oceans and inland waters. In addition, super-resolution occurs mainly on pixels with significant $K_d(490)$ and Chl-a spatial features, especially on the feature edges and locations with a large gradient. Overall, however, there are few differences on average between the original (750 m) $K_d(490)$ and Chl-a images and the super-resolved (375 m) images in moderately and highly turbid coastal oceans and inland waters, showing that the super-resolution process does not change the mean values of the original ocean color product images.

4. Discussions and Conclusions

As satellite images from more sensors have become available, there are now many research activities dedicated to super-resolving remote sensing images. Liu and Wang (2021) [16] used the deep CNN to sharpen VIIRS M-band $nL_w(\lambda)$ images using the high-spatial resolution features from I1-band $nL_w(638)$ data. While $nL_w(\lambda)$ spectra of the five M-bands are primary parameters directly derived from VIIRS measurements, ocean/water biological and biogeochemical products Chl-a and $K_d(490)$ are important water property data and have been widely used in the science and user communities for various research and applications [47–50]. In this study, we further develop and evaluate high-resolution Chl-a and $K_d(490)$ products based on super-resolved VIIRS $nL_w(\lambda)$ images of the five M-bands. The deep CNN method is retrained with the training dataset from the Bohai Sea, Baltic Sea, and La Plata River Estuary as well, so that the performance of networks is

significantly improved over extremely turbid coastal oceans and inland waters. In fact, the new trained networks, which cover wide water optical types, are generally applicable to various highly turbid coastal oceans and inland waters (other than the region with the training dataset). Indeed, the evaluation results show that a super-resolved $K_d(490)$ image is much sharper than the original one, and has more detailed fine spatial structures. Although Chl-a features look different from $K_d(490)$ (as expected), the fine spatial features are also enhanced in the super-resolved Chl-a images. The high $K_d(490)$ and Chl-a filaments are much sharper and thinner in the super-resolved images, and some of the finer features that are not available in the original (750 m) images now appear in the super-resolved (375 m) images. The networks are also tested in four other coastal and inland waters. The evaluation results show that the super-resolution occurs mainly on pixels of $K_d(490)$ and Chl-a spatial features (i.e., spatial variations), especially on the feature edges and locations with a large spatial gradient. It is also concluded that the super-resolution process does not change the mean value of the original images, while adding high-frequency features in the super-resolved water property product images.

It should be noted that the high-resolution $K_d(490)$ and Chl-a images are derived from super-resolved $nL_w(\lambda)$ spectra images. As analyzed in Liu and Wang (2021) [16], the high-spatial resolution I1 band, $nL_w(638)$, is highly correlated to $nL_w(\lambda)$ of the VIIRS five M-bands, so that the networks are trained to extract high-frequency variations from $nL_w(\lambda)$ at the I1 band and transfer to those at M-bands. However, both $K_d(490)$ and Chl-a algorithms use $nL_w(\lambda)$ at multi-spectral bands, and their relationships to that at the I1 band are not linear [7,9]. As can be seen in Figure 4, $K_d(490)$ and Chl-a images usually show different patterns owing to differences in the algorithms, which indicate that they are not directly correlated. Thus, directly super-resolving $K_d(490)$ and Chl-a images from coarse resolution to fine resolution is not as effective as that for $nL_w(\lambda)$. In fact, the evaluation results show that super-resolved $nL_w(\lambda)$ at the VIIRS five M-bands are quite accurate [16] and, consequently, VIIRS-derived $K_d(490)$ and Chl-a images from super-resolved $nL_w(\lambda)$ spectra perform better than those from the direct super-resolution approach for $K_d(490)$ and Chl-a.

It is also noted that the networks have the limitation when they are applied to super-resolve ocean color images in clear open ocean. Owing to the sensor characteristics, $nL_w(638)$ data generally have very weak signals with noticeable noise in the clear open ocean. Consequently, the networks add the data noise in the super-resolved $nL_w(\lambda)$, $K_d(490)$, and Chl-a images. For example, in the open ocean outside of the Chesapeake Bay (Figure 8) and in the Gulf of Mexico (Figure 10), the value of $K_d(490)$ is ~0.1 m^{-1}, and the super-resolved $K_d(490)$ and Chl-a images show some noise on the lower-right corner.

Because the performance of the deep CNN relies on the training dataset, it is recommended to verify and validate the super-resolved images when the networks are applied to other coastal and inland water regions, although the results show that the networks are also applicable to various coastal and inland water regions (different from the training dataset). Coastal and inland waters around the world generally show different optical properties owing to various suspended particulate matter types (e.g., sediment, phytoplankton, colored dissolved organic matter, and so on) as well as concentrations, which lead to complex M-band $nL_w(\lambda)$ spectra in VIIRS ocean color images. Abnormal $nL_w(\lambda)$ outside the range of the training dataset could result in inaccurate super-resolution in $nL_w(\lambda)$, $K_d(490)$, and Chl-a images. The water turbidity seems to be an important factor that affects the super-resolution process. In our studies, the validation results indeed show that the networks with *old training* underestimate $nL_w(551)$ and Chl-a in the La Plata River Estuary and the upper Chesapeake Bay region. By including the La Plata River Estuary data in the training dataset (*new training*), it not only resolves the discrepancies in the La Plata River Estuary, but also in the highly turbid upper Chesapeake Bay region. Therefore, it is important to include various water types in the training dataset. We emphasize that it is not necessary to include all coastal/inland water data for the training, rather it is important

to evaluate and validate the super-resolved images when the networks are applied to a new region of interest.

In the case of a discrepancy found between the super-resolved and original images when applied to a new region, network models need to be re-trained by including data of the region (or water type) in the training dataset. Fortunately, re-training the networks does not mean restarting from scratch. Instead, the networks can be trained incrementally, i.e., starting from the previously trained CNN weights, and re-training with only the new data. With this approach, the computation time to train with new dataset is significantly reduced, while the networks still retain all previously learned skills. By adding more and more data to the training dataset, the network model weights are gradually fine-tuned, and the network eventually will have the skills to super-resolve ocean color images of global coastal oceans and inland waters. Furthermore, we can also train the networks to utilize $nL_w(\lambda)$ spectra with high resolution images from many other satellite sensors. For example, OLCI on the Sentinel-3A/3B has spatial resolution of 300 m, and the Operational Land Imager (OLI) on Landsat-8 has spatial resolution of 30 m. In fact, the networks have the capability to simultaneously super-resolve high resolution ocean color data from multiple sources of different satellite sensors. Therefore, the high-spatial resolution imageries from multi-sensors and multi-bands can be fused into networks to conduct the super-resolving ocean color data processing.

References

1. Gordon, H.R.; Wang, M. Retrieval of water-leaving radiance and aerosol optical thickness over the oceans with seawifs: A preliminary algorithm. *Appl. Opt.* **1994**, *33*, 443–452. [CrossRef]
2. IOCCG. Atmospheric correction for remotely-sensed ocean-colour products. In *Reports of the International Ocean-Colour Coordinating Group*; No., 10; Wang, M., Ed.; IOCCG: Dartmouth, NS, Canada, 2000. [CrossRef]
3. Wang, M. Remote sensing of the ocean contributions from ultraviolet to near-infrared using the shortwave infrared bands: Simulations. *Appl. Opt.* **2007**, *46*, 1535–1547. [CrossRef]
4. Wang, M.; Jiang, L. VIIRS-derived ocean color product using the imaging bands. *Remote Sens. Environ.* **2018**, *206*, 275–286. [CrossRef]
5. O'Reilly, J.E.; Maritorena, S.; Mitchell, B.G.; Siegel, D.A.; Carder, K.L.; Garver, S.A.; Kahru, M.; McClain, C.R. Ocean color chlorophyll algorithms for SeaWiFS. *J. Geophys. Res.* **1998**, *103*, 24937–24953. [CrossRef]
6. Hu, C.; Lee, Z.; Franz, B.A. Chlorophyll a algorithms for oligotrophic oceans: A novel approach based on three-band reflectance difference. *J. Geophys. Res.* **2012**, *117*, C01011. [CrossRef]
7. Wang, M.; Son, S. VIIRS-derived chlorophyll-a using the ocean color index method. *Remote Sens. Environ.* **2016**, *182*, 141–149. [CrossRef]
8. O'Reilly, J.E.; Werdell, P.J. Chlorophyll algorithms for ocean color sensors—OC4, OC5 & OC6. *Remote Sens. Environ.* **2019**, *229*, 32–47.
9. Wang, M.; Son, S.; Harding, L.W., Jr. Retrieval of diffuse attenuation coefficient in the Chesapeake Bay and turbid ocean regions for satellite ocean color applications. *J. Geophys. Res.* **2009**, *114*, C10011. [CrossRef]
10. Lee, Z.P.; Carder, K.L.; Arnone, R.A. Deriving inherent optical properties from water color: A multiple quasi-analytical algorithm for optically deep waters. *Appl. Opt.* **2002**, *41*, 5755–5772. [CrossRef]
11. Shi, W.; Wang, M. A blended inherent optical property algorithm for global satellite ocean color observations. *Limnol. Oceanogr. Methods* **2019**, *17*, 377–394. [CrossRef]
12. Werdell, P.J.; Franz, B.A.; Bailey, S.W.; Feldman, G.C.; Boss, E.; Brando, V.E.; Dowell, M.; Hirata, T.; Lavender, S.J.; Lee, Z.P.; et al. Generalized ocean color inversion model for retrieving marine inherent optical properties. *Appl. Opt.* **2013**, *52*, 2019–2037. [CrossRef]

13. Wang, M.; Liu, X.; Tan, L.; Jiang, L.; Son, S.; Shi, W.; Rausch, K.; Voss, K. Impact of VIIRS SDR performance on ocean color products. *J. Geophys. Res. Atmos.* **2013**, *118*, 10347–10360. [CrossRef]

14. Wang, M.; Isaacman, A.; Franz, B.A.; McClain, C.R. Ocean color optical property data derived from the Japanese Ocean Color and Temperature Scanner and the French Polarization and Directionality of the Earth's Reflectances: A comparison study. *Appl. Opt.* **2002**, *41*, 974–990. [CrossRef]

15. Goldberg, M.D.; Kilcoyne, H.; Cikanek, H.; Mehta, A. Joint Polar Satellite System: The United States next generation civilian polar-orbiting environmental satellite system. *J. Geophys. Res. Atmos.* **2013**, *118*, 13463–13475. [CrossRef]

16. Liu, X.; Wang, M. Super-resolution of VIIRS-measured ocean color products using deep convolutional neural network. *IEEE Trans. Geosci. Remote Sens.* **2021**, *59*, 114–127. [CrossRef]

17. Aiazzi, B.; Baronti, S.; Selva, M. Improving component substitution pansharpening through multivariate regression of MS + Pan data. *IEEE Trans. Geosci. Remote Sens.* **2007**, *45*, 3230–3239. [CrossRef]

18. Atkinson, P.M. Issues of uncertainty in super-resolution mapping and their implications for the design of an inter-comparison study. *Int. J. Remote Sens.* **2009**, *30*, 5293–5308. [CrossRef]

19. Choi, J.; Yu, K.; Kim, Y. A new adaptive component-substitution based satellite image fusion by using partial replacement. *IEEE Trans. Geosci. Remote Sens.* **2011**, *49*, 295–309. [CrossRef]

20. Sales, M.H.R.; Souza, C.M.; Kyriakidis, P.C. Fusion of modis images using kriging with external drift. *IEEE Trans. Geosci. Remote Sens.* **2013**, *51*, 2250–2259. [CrossRef]

21. Vivone, G.; Restaino, R.; Mura, M.D.; Licciardi, G.; Chanussot, J. Contrast and error-based fusion scheme for multispectral image pan-sharpening. *IEEE Geosci. Remote Sens. Lett.* **2014**, *11*, 930–934. [CrossRef]

22. Wang, Q.; Shi, W.; Li, Z.; Atkinson, P.M. Fusion of Sentinel-2 images. *Remote Sens. Environ.* **2016**, *187*, 241–252. [CrossRef]

23. Goodfellow, I.; Bengio, Y.; Courville, A. *Deep Learning*; MIT Press: Cambridge, MA, USA, 2016; Available online: http://www.deeplearningbook.org/ (accessed on 14 May 2021).

24. Gordon, H.R.; Clark, D.K.; Mueller, J.L.; Hovis, W.A. Phytoplankton pigments from the Nimbus-7 Coastal Zone Color Scanner: Comparisons with surface measurements. *Science* **1980**, *210*, 63–66. [CrossRef]

25. Hovis, W.A.; Clark, D.K.; Anderson, F.; Austin, R.W.; Wilson, W.H.; Baker, E.T.; Ball, D.; Gordon, H.R.; Mueller, J.L.; Sayed, S.T.E.; et al. Nimbus 7 Coastal Zone Color Scanner: System description and initial imagery. *Science* **1980**, *210*, 60–63. [CrossRef] [PubMed]

26. McClain, C.R. A decade of satellite ocean color observations. *Annu. Rev. Mar. Sci.* **2009**, *1*, 19–42. [CrossRef]

27. McClain, C.R.; Feldman, G.C.; Hooker, S.B. An overview of the SeaWiFS project and strategies for producing a climate research quality global ocean bio-optical time series. *Deep Sea Res. Part II* **2004**, *51*, 5–42. [CrossRef]

28. Esaias, W.E.; Abbott, M.R.; Barton, I.; Brown, O.B.; Campbell, J.W.; Carder, K.L.; Clark, D.K.; Evans, R.L.; Hodge, F.E.; Gordon, H.R.; et al. An overview of MODIS capabilities for ocean science observations. *IEEE Trans. Geosci. Remote Sens.* **1998**, *36*, 1250–1265. [CrossRef]

29. Salomonson, V.V.; Barnes, W.L.; Maymon, P.W.; Montgomery, H.E.; Ostrow, H. MODIS: Advanced facility instrument for studies of the earth as a system. *IEEE Trans. Geosci. Remote Sens.* **1989**, *27*, 145–153. [CrossRef]

30. Rast, M.; Bezy, J.L.; Bruzzi, S. The ESA Medium Resolution Imaging Spectrometer MERIS a review of the instrument and its mission. *Int. J. Remote Sens.* **1999**, *20*, 1681–1702. [CrossRef]

31. Donlon, C.; Berruti, B.; Buongiorno, A.; Ferreira, M.-H.; Femenias, P.; Frerick, J.; Goryl, P.; Klein, U.; Laur, H.; Mavrocordatos, C.; et al. The Global Monitoring for Environment and Security (GMES) Sentinel-3 mission. *Remote Sens. Environ.* **2012**, *120*, 37–57. [CrossRef]

32. Tanaka, K.; Okamura, Y.; Amano, T.; Hiramatsu, M.; Shiratama, K. Development status of the Second-Generation Global Imager (SGLI) on GCOM-C. In Proceedings of the Sensors, Systems, and Next-Generation Satellites XIII, Berlin, Germany, 22 September 2009; Volume 7474.

33. Shi, W.; Wang, M. An assessment of the black ocean pixel assumption for MODIS SWIR bands. *Remote Sens. Environ.* **2009**, *113*, 1587–1597. [CrossRef]

34. Shi, W.; Wang, M. Characterization of global ocean turbidity from Moderate Resolution Imaging Spectroradiometer ocean color observations. *J. Geophys. Res.* **2010**, *115*, C11022. [CrossRef]

35. Wang, M.; Liu, X.; Jiang, L.; Son, S. *Visible Infrared Imaging Radiometer Suite Ocean Color Products. VIIRS Ocean Color Algorithm Theoretical Basis Document*; NOAA/NESDIS/STAR: Maryland, USA, 2017. Available online: https://www.star.nesdis.noaa.gov/jpss/documents/ATBD/ATBD_OceanColor_v1.0.pdf (accessed on 14 May 2021).

36. Jiang, L.; Wang, M. Improved near-infrared ocean reflectance correction algorithm for satellite ocean color data processing. *Opt. Express* **2014**, *22*, 21657–21678. [CrossRef]

37. Wang, M.; Shi, W. The NIR-SWIR combined atmospheric correction approach for MODIS ocean color data processing. *Opt. Express* **2007**, *15*, 15722–15733. [CrossRef] [PubMed]

38. Wang, M.; Shi, W. Estimation of ocean contribution at the MODIS near-infrared wavelengths along the east coast of the U.S.: Two case studies. *Geophys. Res. Lett.* **2005**, *32*, L13606. [CrossRef]

39. Wang, M.; Son, S.; Shi, W. Evaluation of MODIS SWIR and NIR-SWIR atmospheric correction algorithm using SeaBASS data. *Remote Sens. Environ.* **2009**, *113*, 635–644. [CrossRef]

40. Wang, M.; Tang, J.; Shi, W. MODIS-derived ocean color products along the China east coastal region. *Geophy. Res. Lett.* **2007**, *34*, L06611. [CrossRef]
41. Wang, M.; Shi, W.; Tang, J. Water property monitoring and assessment for China's inland Lake Taihu from MODIS-Aqua measurements. *Remote Sens. Environ.* **2011**, *115*, 841–854. [CrossRef]
42. Morel, A.; Gentili, G. Diffuse reflectance of oceanic waters. III. Implication of bidirectionality for the remote-sensing problem. *Appl. Opt.* **1996**, *35*, 4850–4862. [CrossRef]
43. Gordon, H.R. Normalized water-leaving radiance: Revisiting the influence of surface roughness. *Appl. Opt.* **2005**, *44*, 241–248. [CrossRef]
44. Wang, M. Effects of ocean surface reflectance variation with solar elevation on normalized water-leaving radiance. *Appl. Opt.* **2006**, *45*, 4122–4128. [CrossRef] [PubMed]
45. Wei, J.; Wang, M.; Lee, Z.; Briceño, H.O.; Yu, X.; Jiang, L.; Garcia, R.; Wang, J.; Luis, K. Shallow water bathymetry with multi-spectral satellite ocean color sensors: Leveraging temporal variation in image data. *Remote Sens. Environ.* **2020**, *250*, 112035. [CrossRef]
46. IOCCG. Earth observations in support of global water quality monitoring. In *Reports of International Ocean-Color Coordinating Group*; No.17; Greb, S., Dekker, A., Binding, C., Eds.; IOCCG: Dartmouth, NS, Canada, 2018. [CrossRef]
47. Behrenfeld, M.J.; Falkowski, P.G. Photosynthetic rates derived from satellite-based chlorophyll concentration. *Limnol. Oceanogr.* **1997**, *42*, 1–20. [CrossRef]
48. Son, S.; Wang, M.; Harding, L.W., Jr. Satellite-measured net primary production in the Chesapeake Bay. *Remote Sens. Environ.* **2014**, *144*, 109–119. [CrossRef]
49. Tomlinson, M.C.; Stumpf, R.P.; Ransibrahmanakul, V.; Truby, E.W.; Kirkpatrick, G.J.; Pederson, B.A.; Vargo, G.A.; Heil, C.A. Evaluation of the use of SeaWiFS imagery for detecting *Karenia Brevis* harmful algal blooms in the eastern Gulf of Mexico. *Remote Sens. Environ.* **2004**, *91*, 293–303. [CrossRef]
50. Stumpf, R.P.; Culver, M.E.; Tester, P.A.; Kirkpatrick, G.J.; Pederson, B.; Tomlinson, M.C.; Truby, E.; Ransibrahmanakul, V.; Hughes, K.; Soracco, M. Use of satellite imagery and other data for monitoring *Karenia Brevis* blooms in the Gulf of Mexico. *Harmful Algae* **2003**, *2*, 147–160. [CrossRef]
51. Lanaras, C.; Bioucas-Dias, J.; Galliani, S.; Baltsavias, E.; Schindler, K. Super-resolution of Ssentinel-2 images: Learning a globally applicable deep neural network. *ISPRS J. Photogramm. Remote Sens.* **2018**, *146*, 305–319. [CrossRef]
52. He, K.; Zhang, X.; Ren, S.; Sun, J. Deep residual learning for image recognition. In Proceedings of the IEEE conference on computer vision and pattern Recognition (CVPR), Silver Spring, MD, USA, 27–30 June 2016; pp. 770–778.
53. Dogliotti, A.I.; Ruddick, K.; Guerrero, R. Seasonal and inter-annual turbidity variability in the Rio de La Plata from 15 years of MODIS: El Nino dilution effect. *Estuar. Coast. Shelf Sci.* **2016**, *182*, 27–39. [CrossRef]
54. Shi, W.; Wang, M. Water properties in the La Plata River Estuary from VIIRS observations. *Continent. Shelf Res.* **2020**, *198*, 104100. [CrossRef]
55. Shechtman, E.; Irani, M. Matching local self-similarities across images and videos. In Proceedings of the IEEE Conference on Computer Vision and Pattern Recognition, Minneapolis, MN, USA, 17–22 June 2007. [CrossRef]
56. Glasner, D.; Bagon, S.; Irani, M. Super-resolution from a single image. In Proceedings of the 2009 IEEE 12th International Conference on Computer Vision, Kyoto, Japan, 29 September–2 October 2009; pp. 349–356.
57. Shi, W.; Wang, M. Ocean reflectance spectra at the red, near-infrared, and shortwave infrared from highly turbid waters: A study in the Bohai Sea, Yellow Sea, and East China Sea. *Limnol. Oceanogr.* **2014**, *59*, 427–444. [CrossRef]
58. Shi, W.; Wang, M. Satellite views of the Bohai Sea, Yellow Sea, and East China Sea. *Prog. Oceanogr.* **2012**, *104*, 35–45. [CrossRef]
59. Shi, W.; Wang, M.; Jiang, L. Spring-neap tidal effects on satellite ocean color observations in the Bohai Sea, Yellow Sea, and East China Sea. *J. Geophys. Res.* **2011**, *116*, C12032. [CrossRef]
60. Shi, W.; Wang, M.; Li, X.; Pichel, W.G. Ocean sand ridge signatures in the Bohai Sea observed by satellite ocean color and synthetic aperture radar measurements. *Remote Sens. Environ.* **2011**, *115*, 1926–1934. [CrossRef]
61. Schubel, J.R.; Pritchard, D.W. Responses of upper Chesapeake Bay to variations in discharge of the Susquehanna River. *Estuaries* **1986**, *9*, 236–249. [CrossRef]
62. Shi, W.; Wang, M.; Jiang, L. Tidal effects on ecosystem variability in the Chesapeake Bay from MODIS-Aqua. *Remote Sens. Environ.* **2013**, *138*, 65–76. [CrossRef]
63. Liu, X.; Wang, M. River runoff effect on the suspended sediment property in the upper Chesapeake Bay using MODIS observations and ROMS simulations. *J. Geophys. Res. Oceans* **2014**, *119*, 8646–8661. [CrossRef]
64. Son, S.; Wang, M. Water quality properties derived from VIIRS measurements in the Great Lakes. *Remote Sens.* **2020**, *12*, 1605. [CrossRef]
65. Son, S.; Wang, M. VIIRS-derived water turbidity in the Great Lakes. *Remote Sens.* **2019**, *11*, 1448. [CrossRef]
66. Watson, S.B.; Miller, C.; Arhonditsis, G.; Boyer, G.L.; Carmichael, W.; Charlton, M.N.; Confesor, R.; Depew, D.C.; Hook, T.O.; Ludsin, S.A.; et al. The re-eutrophication of Lake Erie: Harmful algal blooms and hypoxia. *Harmful Algae* **2016**, *56*, 44–66. [CrossRef]
67. Michalak, A.M.; Anderson, E.J.; Beletsky, D.; Boland, S.; Bosch, N.S.; Bridgeman, T.T.; Chaffin, J.D.; Cho, K.; Confesor, R.; Daloglu, I.; et al. Record-setting algal blooms in Lake Erie caused by agricultural and meteorological trends consisten with expected future conditions. *Proc. Natl. Acad. Sci. USA* **2013**, *110*, 6448–6452. [CrossRef]

68. Steffen, M.M.; Belisle, S.; Watson, S.B.; Boyer, G.L.; Wilhelm, S.W. Status, causes and controls of cyanobacterial blooms in Lake Erie. *J. Great Lakes Res.* **2014**, *40*, 215–225. [CrossRef]
69. Moore, T.S.; Mouw, C.B.; Sullivan, J.M.; Twardowski, M.S.; Burtner, A.M.; Ciochetto, A.B.; McFarland, M.N.; Nayak, A.R.; Paladino, D.; Stockley, N.D.; et al. Bio-optical properties of cyanobacteria blooms in western Lake Erie. *Front. Mar. Sci.* **2017**, *4*, 300. [CrossRef]
70. Milliman, J.D.; Meade, R.H. World-wide delivery of river sediment to the oceans. *J. Geol.* **1983**, *91*, 1–21. [CrossRef]
71. Meade, R.H.; Parker, R.S. Sediment in Rivers of the United States. In *National Water Summary 1984*; U.S. Geological Survey Water Supply Paper; U.S. Geological Survey: Reston, VA, USA, 1985; p. 49. [CrossRef]
72. Shi, W.; Wang, M. Satellite observations of flood-driven Mississippi River plume in the spring of 2008. *Geophy. Res. Lett.* **2009**, *36*, L07607. [CrossRef]